High-Performance Thermoelectric Oxides Based on Spinel Structure

M. Hussein N. Assadi*

School of Materials Science and Engineering, UNSW Sydney, NSW, 2052, Australia.

J. Julio Gutiérrez Moreno

Institute for Advanced Study, Shenzhen University, Shenzhen 518060, China, and
Key Laboratory of Optoelectronic Devices and Systems of Ministry of Education and Guangdong Province,
College of Physics and Optoelectronic Engineering, Shenzhen University, Shenzhen 518060, China.

Marco Fronzi

School of Mathematical and Physical Science, University of Technology Sydney, Sydney, NSW 2007, Australia.
(Dated: 2020)

High-performance thermoelectric oxides could offer a great energy solution for integrated and embedded applications in sensing and electronics industries. Oxides, however, often suffer from low Seebeck coefficient when compared with other classes of thermoelectric materials. In search of high-performance thermoelectric oxides, we present a comprehensive density functional investigation, based on GGA+U formalism, surveying the 3d and 4d transition-metal-containing ferrites of the spinel structure. Consequently, we predict $MnFe_2O_4$ and $RhFe_2O_4$ have Seebeck coefficients of $\sim \pm 600\,\mu V\,K^{-1}$ at near room temperature, achieved by light hole and electron doping. Furthermore, $CrFe_2O_4$ and $MoFe_2O_4$ have even higher ambient Seebeck coefficients at $\sim \pm 700\,\mu V\,K^{-1}$. In the latter compounds, the Seebeck coefficient is approximately a flat function of temperature up to ~ 700 K, offering a tremendous operational convenience. Additionally, $MoFe_2O_4$ doped with 10^{19} holes /cm^3 has a calculated thermoelectric power factor of 689.81 $\mu W\,K^{-2}\,m^{-1}$ at 300 K, and 455.67 $\mu W\,K^{-2}\,m^{-1}$ at 600 K. The thermoelectric properties predicted here can bring these thermoelectric oxides to applications at lower temperatures traditionally fulfilled by more toxic and otherwise burdensome materials.

Keywords: thermoelectric oxides, $MoFe_2O_4$, $CrFe_2O_4$, ferrites, spinels, high Seebeck coefficient, density functional theory, Boltzmann transport equation.

I. INTRODUCTION

Thermoelectric (TE) materials[1–3] have the potential to fulfill a grand promise for a variety of applications from recovering waste heat in industrial processes[4,5] to powering small autonomous sensors and devices.[6] Currently, a wide range of materials including complex chalcogenides[7] (compounds containing group VIA elements), skutterudites[8] (As-based compounds), half-Heusler alloys[9–11] (ternary cubic metallic alloys), silicon-germanium based compounds[12,13] are considered to be the best performing TE materials. Each class of these TE materials, however, suffers from some shortcomings. Examples include the instability and Se loss throughout the heating/cooling cycles for chalcogenides $CuSe_2$[14] and $SnSe$,[15] the low or asymmetric dopability in $ZnSb$[16,17] and Mg_2Si[18], and the criticality and toxicity of Te and Pb in $PbTe$,[19] to mention few common TE compounds. One plausible solution to circumvent most of these problems is developing oxide thermoelectric materials. Oxides, having dominantly ionic characters, are chemically more suitable than other thermoelectric materials by two means: (a) a wide range of elements can be doped into these materials; (b) they have higher chemical stability in oxidizing environments. Furthermore, the top-performing oxide thermoelectric materials enjoy the potential of seamless integration with the current oxide electronics[20] for embedded applications,[21] an advantage not shared with other class of TE materials that require fundamentally different synthesis techniques.

In thermoelectric materials, the Seebeck effect[22] refers to an electric potential difference (ΔV) created by a temperature gradient (ΔT) across the length of the material itself and quantified by the Seebeck coefficient $S = -\Delta V / \Delta T$ which is commonly measured in $\mu V\,K^{-1}$. S is related to the TE figure of merit (ZT), which determines the thermoelectric efficiency of a material by $ZT = S^2 \sigma T / \kappa$, where σ is the electrical conductivity, T is the absolute temperature, and κ is the thermal conductivity of which the electronic contribution is denoted κ_e. One of the easiest ways to maximize the thermoelectric ZT is first to identify materials with high S, and subsequently enhance S through elemental doping. Optimizing ZT is a challenge in itself due to the interdependence of S, σ, and κ. Many industrial applications also require the thermoelectric materials to maintain their ZT during the operation at varying temperature ranges and when under stress.[23,24] Consequently, many factors must be carefully taken into account and fine-tuned in designing new thermoelectric oxides. Given the complexity of such a design, an experimental approach based on judicious guesswork followed by trial and error is cost-prohibitive.

Computational screening has recently emerged as a novel tool in the discovery of brand-new thermoelectric

materials.[25–30] Subsequently, through computational survey into uncharted materials territory, one may find a desirable oxide alternative to the common thermoelectric materials, at least for those applications where exposure to elements is inevitable. More specifically, our study was motivated by the recent prediction,[31] and observation[32] of spinel oxides with high Seebeck coefficient, and high-performance thermoelectric cubic oxides.[33] Therefore, in this work, we surveyed a specific class of spinel ferrites, isomorphic to magnetite, in search of high S. In particular, our survey spanned twelve 3d and 4d transition metal (TM) containing spinel ferrites, where the TM ions are tetrahedrally coordinated by O, A site, while the Fe ions are octahedrally coordinated, B site (Figure 1).

II.   COMPUTATIONAL SETTINGS

We carried out spin-polarized density functional theory (DFT) calculations within the projector augmented wave formalism[34] as implemented in VASP code[35,36] with an energy cut-off of 520 eV for geometry optimization. At this stage, we used a Brillouin zone sampling of a mesh generated by $9 \times 9 \times 9$ Monkhorst-Pack grid to relax the primitive cell (Figure 1b) of the $TMFe_2O_4$ compounds to forces smaller than 0.01 eV Å^{-1}. We also applied a GGA+U correction[37,38] with an on-site Coulomb interaction term of $U = 3.5$ eV and on-site exchange interaction of $J = 0.5$ eV for all 3d TM ions, and $U = 3$ eV and $J = 1$ eV o for all 4d TM ions to improve the electronic description arising from the strong localization of d electrons throughout all calculations. These U_{eff} values reproduce the measured magnetic ordering and the electronic structure for Fe_3O_4[39] and $MoFe_2O_4$.[40] The validity of these U and J values were examined and confirmed in **Figures S1**–**S3**. Furthermore, the use of a uniform U and J values for all 3d and 4d TM ions offers a straightforward comparison within the entire materials family.[41] The structural descriptions and the proof of the stability of the antiferromagnetic phase of the compounds studied here have been published elsewhere.[42] The elastic tensor was calculated using conventional $Fd\bar{3}m$ unitcell containing 56 atoms based on the strain-stress method as implemented in VASP[43] and extracted using MechElastic script.[44] We employed central differences with a step size of 0.015 Å.

For calculating the density of states (DOS) and the transport properties, we used an ultra-fine $20\times20\times20$ Monkhorst-Pack grid in conjunction with an energy cut-off of 650 eV. This Monkhorst-Pack grid generated 7700 unique irreducible k-points with a tight spacing of ~ 0.01 Å^{-1}. To ensure the ultimate accuracy, for smearing, we utilized the tetrahedron method with Blchl correction. We then calculated the Seebeck coefficient using the BoltzTraP2 code,[45] which solves the linearized Boltzmann transport equation within the constant relaxation time (τ) approximation, in which τ is assumed to be independent of temperature (T) and electron's energy (E). BoltzTrap2, therefore, only relies on the DFT calculated band and k-dependent quasiparticle eigenvalues as input. The assumption of a T and E independent τ results in a simple and tractable form of the equations for S, σ and κ_{e}.[46] The constant relaxation time approximation, despite its simplicity, predicts S values that match well with experiments, and is widely adopted in the high throughput theoretical search of novel thermoelectric materials.[29,47] The success of this approximation may stem from the fact that in doped semiconductors, such as the ones discussed here, carriers' relaxation time (and mobility) does vary very little with temperatures near and above ambient.[48–50] Constant relaxation time approximation, however, fails to describe the Seebeck coefficient for those materials in which the electron relaxation time is strongly energy-dependent such as Li.[51] In Li the rapidly increasing DOS across the Fermi energy is the cause of the deviation from constant relaxation time approximation.
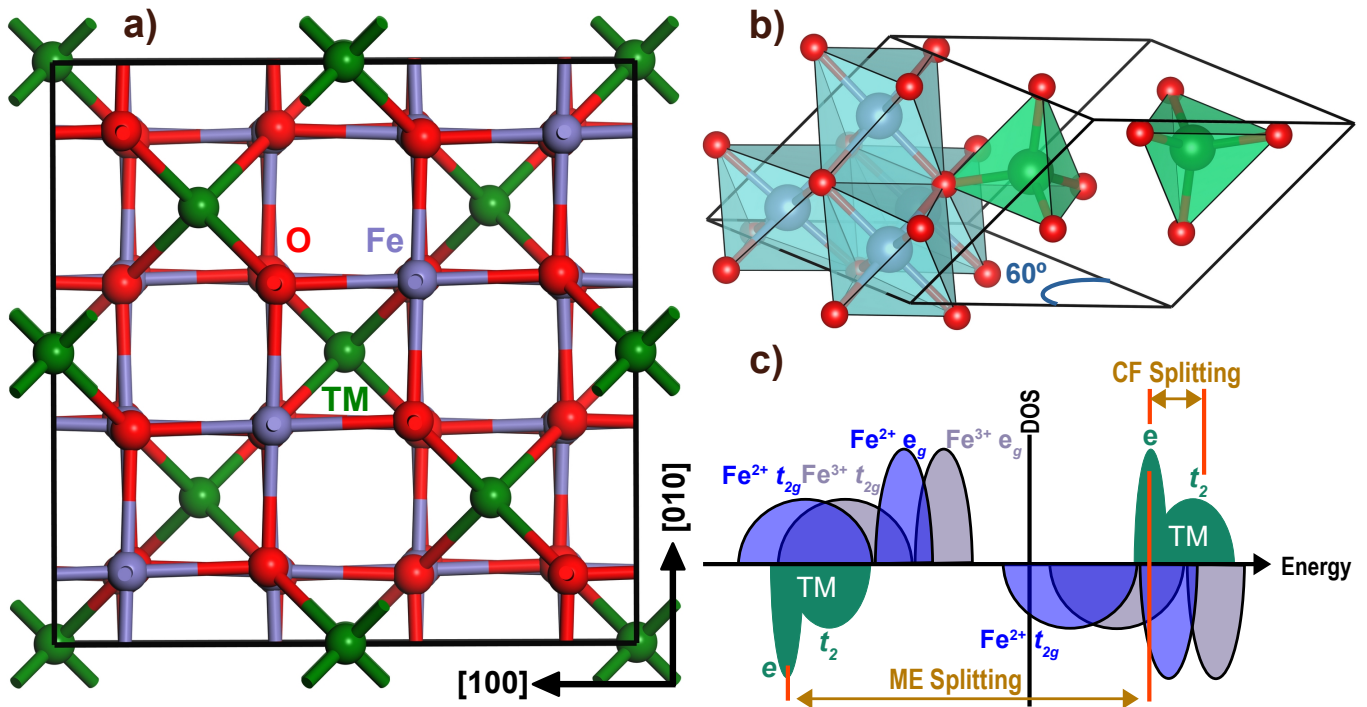
Figure 1. (a) The schematic presentation of the cubic (conventional) $Fd\bar{3}m$ cell of the $TMFe_2O_4$ compounds. (b) Primitive cell of the same structure in the polyhedron presentation. The TM ions are tetrahedrally coordinated while the Fe ions are octahedrally coordinated. (c) The schematic density of states of the representative Fe_3O_4 structure. Crystal field (CF) and the magnetic exchange (ME) are also demonstrated. For other compounds, the partial density of states of the octahedrally coordinated TM cations moves closer to the Fermi level based on occupancy.

III. RESULTS AND DISCUSSION

A. Search for Flat Band

Based on the energy-independent carrier relaxation time and parabolic band approximations, the Seebeck coefficient of a TE material is approximately proportional to the density-of-states effective mass (m_D^*).[52,53] Higher m_D^* originate from sharp peaks in the density of state (DOS) near band edges which indicate flat and dispersionless bands.[54,55] Therefore, in this section, we examine the DOS of the 3d TM and 4d TM containing $TMFe_2O_4$ compounds.

Figure 2 shows the DOS of the 3d TM containing $TMFe_2O_4$ compounds. One general feature in all compounds is a sizeable magnetic exchange that separates the spin-up ($\uparrow$) channels from the spin-down ($\downarrow$) channels. Moreover, for the octahedrally coordinated Fe ions, the crystal field splits each spin channel into lower triply degenerate t_{2g} and higher doubly degenerate e_g states. For the tetrahedrally coordinated TM ions, this splitting is reversed to lower doubly degenerate e and higher triply degenerate t_2 states. A schematic of the splittings is provided in Figure 1c. As seen in Figure 2, Fe ions in all $TMFe_2O_4$ undergo a charge disproportionation into Fe^{3+} and Fe^{2+}, except in $MnFe_2O_4$, which will be discussed shortly. For the high-spin Fe^{3+}, the spin-up channel of the t_{2g} and e_g states (indicated with blue lines) are all filled and located at the bottom of the valence band (~ -8 eV $< E < \sim -6$ eV), while the spin-down channel is completely empty. For the high-spin Fe^{2+} ions, one electron, however, occupies the spin-down t_{2g} states, which are marked with blue arrows in Figure 2. Given the dominance of this peak at the valence band top, its vicinity to the Fermi level, and its sharpness can determine S.

Fe charge disproportionation in the majority of the 3d $TMFe_2O_4$ compounds dictates that all the tetrahedral TM ions are of +3 oxidation state except for Mn. In $MnFe_2O_4$, Mn adopts the more stable Mn^{2+} state leaving all Fe in the +3 oxidation state. Consequently, one spin channel of each of the Mn ($e^2 \downarrow t_2^3 \downarrow$) and Fe ($t_{2g}^3 \uparrow e_g^2 \uparrow$) ions become fully occupied, while the respective opposite channels, which are separated by a magnetic exchange interaction, remain empty. Such an electronic configuration, which agrees rather well with earlier computational investigations,[56] creates a gap of 0.59 eV, which is marked with a black bar in Figure 2c.

Moreover, in all 3d $TMFe_2O_4$ compounds, the TM ions have their e and the t_2 states progressively filled. As marked

with a green arrow in Figure 2a, for VFe$_2$O$_4$, V^{3+} has an electronic configuration of $e^2 t_2^0$ of which the e^2 electrons occupy the top of the valence band at ~ -1.2 eV and oppose the spin direction of the filled Fe states constituting a ferrimagnetic alignment. As the 3d TM ions move along the row and more electrons occupy the spin-down of e and t_2 states, the occupied TM electrons move to lower energies. This trend is more evident in Fe$_3$O$_4$ (Figure 2d) than in all other compounds for which the filled $e^2 t_2^3$ states of the tetrahedral Fe are almost at the same energy level as the filled $t_{2g}^3 e_g^2$ states of the octahedral Fe^{3+} at the bottom of the valence band (~ -7 eV). For CoFe$_2$O$_4$ and NiFe$_2$O$_4$, the spin-down channel of Co and Ni remains at the bottom of the valence band while the spin-up channel gets progressively filled as marked with green circles in Figure 2e and Figure 2f.

The DOS for the 4d TMFe$_2$O$_4$ compounds, presented in Figure 3, shows several similarities with those of the 3d counterparts; First, the Fe ions are all in high-spin state and experience a sizeable magnetic exchange; Second, the Fermi level is dominated by the spin-down t_{2g} states of the Fe^{2+} ions (marked with blue arrows) except for the latter RhFe$_2$O$_4$ and PdFe$_2$O$_4$; Third, the 4d TM ions adopt an antiferromagnetic alignment to the Fe ions. The DOS of the 4d TMFe$_2$O$_4$ compounds, however, differ noticeably from those of the 3d containing TMFe$_2$O$_4$ in one aspect, and that is the 4d TM ions have smaller net magnetization than their 3d counterparts. The reduced magnetization can be attributed to the higher TM–O covalency in the case of the 4d elements.[42,57] Additionally, for RhFe$_2$O$_4$ and PdFe$_2$O$_4$, Rh and Pd ions adopt the +2 oxidation state, leaving all Fe ions as Fe^{3+}. Consequently, there are no occupied spin-down Fe t_{2g} states in these compounds below the Fermi level. As shown in Figure 3e, Rh^{2+} adopts the $e^2 \downarrow t_2^3 \downarrow e^2 \uparrow$ electronic configuration. The crystal field splitting between $e \uparrow$ and $t_2 \uparrow$ creates a gap of ~ 0.48 eV, which is marked with a black bar. Pd^{2+}, as shown in Figure 3f, adopts the $e^2 \downarrow t_2^3 \uparrow e^2 \uparrow t_2^1 \uparrow$ electronic configuration, and as a result, the Fermi level lies in the middle of the Pd $t_2 \uparrow$ states. Similar to the 3d TM containing compounds, the shape and position of the spin-down channel of the Fe^{2+} ion may provide the necessary condition for high S in 4d TM based TMFe$_2$O$_4$ compounds.
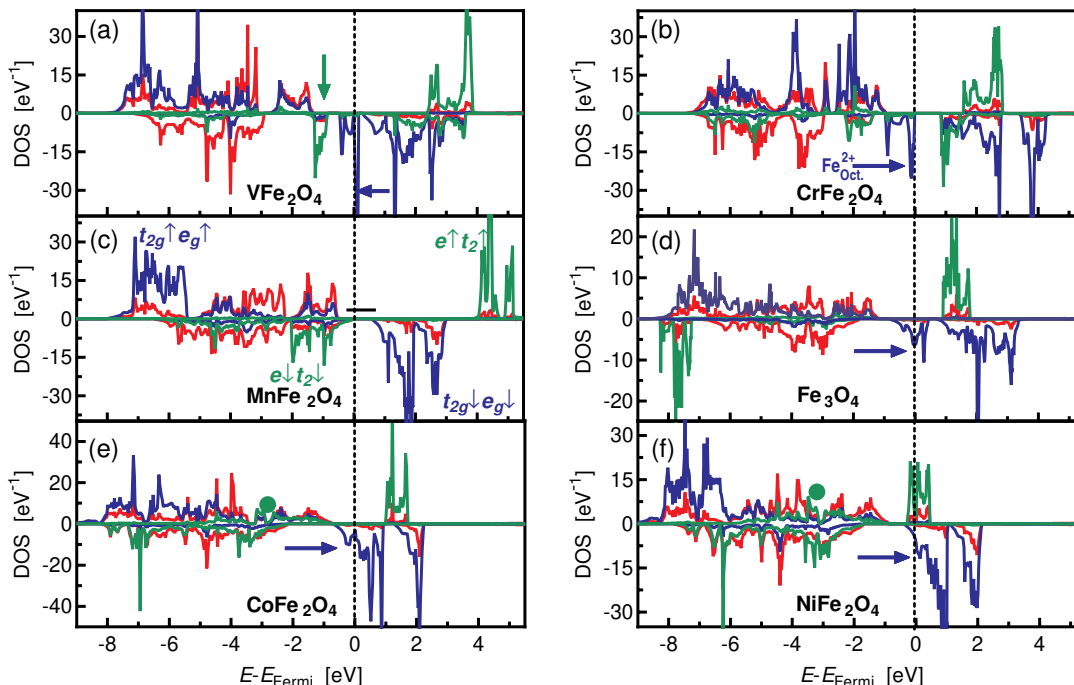

Figure 2. Partial density of states of 3d TM containing-TMFe$_2$O$_4$ compounds. Panels (a) through (f) correspond to VFe$_2$O$_4$ through NiFe$_2$O$_4$, respectively, arranged by TM's atomic number. The blue, green, and red lines denote Fe 3d, TM 3d, and O 2p states, respectively.
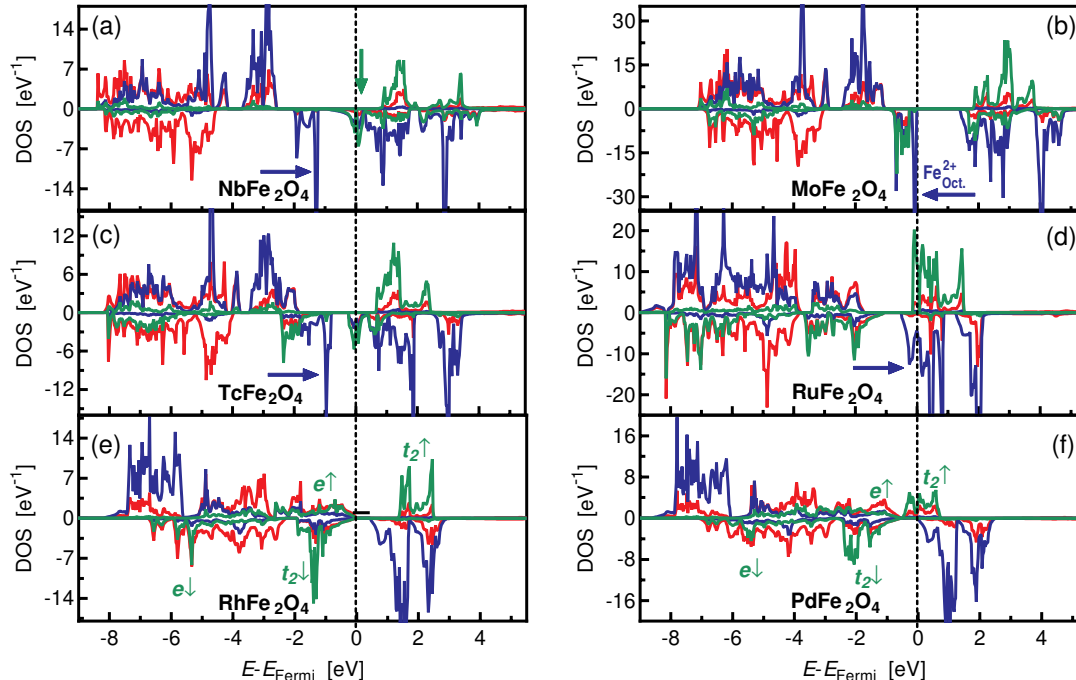
Figure 3. Partial density of states for the 4d TM-containing TMFe$_2$O$_4$ compounds. Panels (a) through (f) correspond to NbFe$_2$O$_4$ through PdFe$_2$O$_4$, respectively, arranged by TM's atomic number. The blue, green, and red lines denote Fe 3d, TM 4d, and O 2p states, respectively.

B.   Thermoelectric Properties

Having the DOS calculated in the previous section, now we present the predicted Seebeck coefficients. The S values as a function of the carrier doping and temperature for 3d and 4d containing TMFe$_2$O$_4$ compounds are presented in Figure 4 and Figure 5, respectively. S values as a function of the shift in the chemical potentials are shown in **Figures S4** and **S5**. For various doping levels, the S value for VFe$_2$O$_4$, Fe$_3$O$_4$, CoFe$_2$O$_4$, NiFe$_2$O$_4$, NbFe$_2$O$_4$, TcFe$_2$O$_4$, RuFe$_2$O$_4$, and PdFe$_2$O$_4$ falls approximately into the interval of ± 150 µV K^{-1}. The DOS indicates that these compounds are metallic or half-metallic, for which the effect of carrier doping is not as potent in influencing S. Among band insulators, MnFe$_2$O$_4$ and RhFe$_2$O$_4$ achieve higher S values of ± 600 µV K^{-1} at 300 K when lightly doped with either n or p carriers at concentrations of 10^{18} and 10^{19} carriers / cm^3. For MnFe$_2$O$_4$ and RhFe$_2$O$_4$, S, nonetheless, falls rapidly with increasing doping level and temperature, especially for $T > 400$ K. The best performing compounds are, however, the remaining band insulators, CrFe$_2$O$_4$, and its 4d counterpart MoFe$_2$O$_4$. For CrFe$_2$O$_4$, at the low 10^{18} cm^{-3} n-type doping, S is -791 µV K^{-1} at $T = 300$ K and reaches a minimum of -819 µV K^{-1} at $T = 450$ K. At the same level of p-type doping, S is 746 µV K^{-1} at $T = 300$ K and peaks to 772 µV K^{-1} at $T = 450$ K. For MoFe$_2$O$_4$, at 10^{18} cm^{-3} of n-type carrier doping, S is -646 µV K^{-1} at $T = 300$ K with a minimum of -779 µV K^{-1} at $T = 850$ K. At the same level of p-type carrier doping, S is 778 µV K^{-1} at $T = 300$ K and peaks at 835 µV K^{-1} at $T = 700$ K. The S values slightly fall by ~ 50 µV K^{-1} for 10^{19} cm^{-3} carrier doping in CrFe$_2$O$_4$ and MoFe$_2$O$_4$. The predicted S values for these compounds are comfortably twice as large as that of Bi$_2$Te$_3$ (~ 250–260 µV K^{-1} at room temperature.)[58,59]

Furthermore, for the best performing CrFe$_2$O$_4$ and MoFe$_2$O$_4$, S falls rapidly with excessive carrier dopings beyond 10^{20} cm^{-3}. For instance, at 10^{22} cm^{-3} of both p and n-type doping, the absolute S value falls to an average of ~ 60 µV K^{-1} in CrFe$_2$O$_4$, and ~ 64 µV K^{-1} in MoFe$_2$O$_4$. The substantial S values in lightly doped CrFe$_2$O$_4$ and MoFe$_2$O$_4$ and their descent for more massive carrier doping stem from the sharp Fe^{2+} 3d peak below the valence band maximum of both compounds—marked with blue arrows in Figure 2b and Figure 3b, respectively. Through light doping, the Fermi level can be ever slightly adjusted so that it falls close to the peak. For instance, in CrFe$_2$O$_4$, 10^{18} cm^{-3} n-type doping shifts the Fermi level -9.90×10^{-4} eV while 10^{22} cm^{-3} n-type doping shifts the Fermi level -1.53 eV at
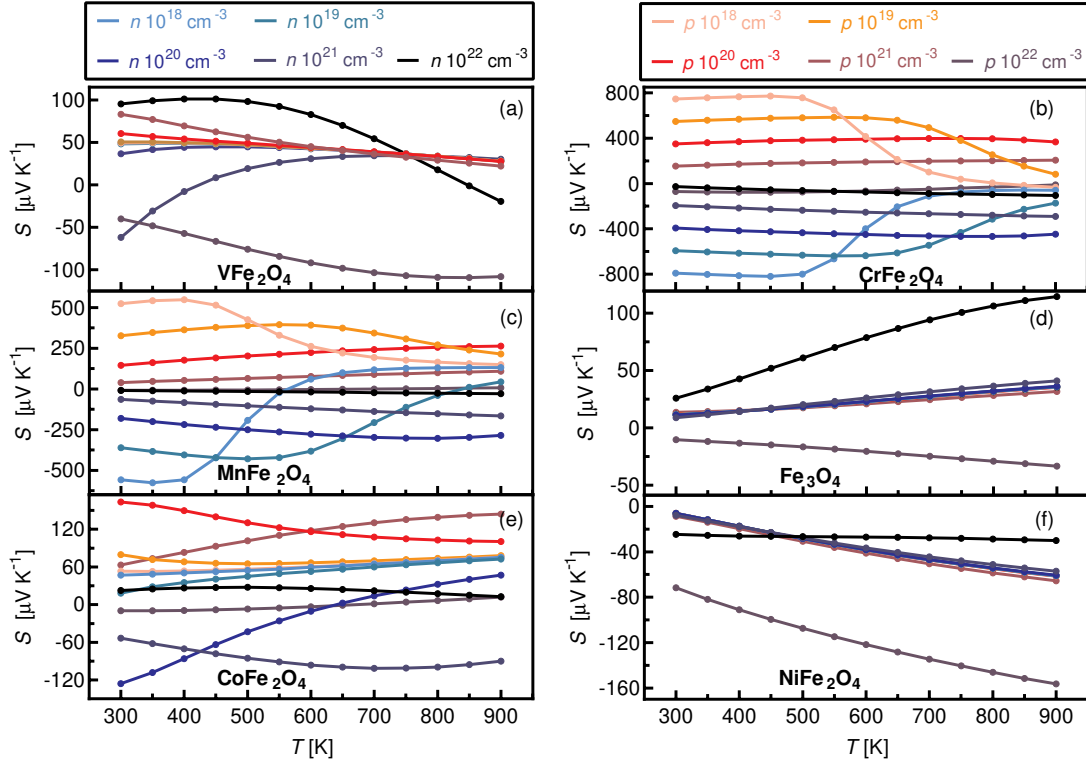
Figure 4. The predicted S values for 3d-based TMFe$_2$O$_4$ compounds as a function of temperature and carrier doping. Panels (a) through (f) correspond to VFe$_2$O$_4$ through NiFe$_2$O$_4$, respectively, arranged by TM's atomic number.

$T = 300$ K. We can, therefore, see that more massive doping moves the Fe 3d peak too far away from the Fermi level and diminishes its favorable effect on S (**Figure S6**). A similar trend can be seen for p-type doping and in MoFe$_2$O$_4$ (**Figure S7**).

C. Best Performing CrFe$_2$O$_4$ and MoFe$_2$O$_4$

Given that in the previous section, we predicted that the semiconducting CrFe$_2$O$_4$ and MoFe$_2$O$_4$ would have the highest Seebeck coefficient among the investigated compounds, their electrical conductivity, and the electronic contribution to the thermal conductivity are examined here. Accordingly, Figure 6 shows κ_e / τ, σ / τ, and PF/τ, for the lightly doped, 10^{19} carriers/cm^3, CrFe$_2$O$_4$, and MoFe$_2$O$_4$. Here, τ is the mean relaxation time used in the BoltzTrap2 calculations. Moreover, we chose to show the results for lightly doped compounds as light doping is easier to achieve experimentally without running into dopant solubility problems. In CrFe$_2$O$_4$, κ_e / τ, σ / τ, PF/τ, for both light hole and light electron doping, have similar values and follow the same trend. κ_e / τ starts at $\sim 1.2 \times 10^{11}$ W m^{-1} K^{-1} s^{-1} at $T = 300$ K and increases sharply by two orders of magnitude with the rising temperature at $T = 900$ K. It is worthy of note that for a compound in which the Fermi level crosses the valence band, such as VFe$_2$O$_4$ of Figure 2a, κ_e / τ is nonetheless two orders of magnitude higher than that of CrFe$_2$O$_4$ at the same doping level (**Figure S8**). σ / τ, after an initial dip, abruptly rises by twofold for $T > \sim 500$ K, indicating a semiconducting behavior. Despite the increase in σ / τ with temperature, PF/τ, nonetheless, drops by ~ 1 order of magnitude from its room temperature value with the rising temperature at $T = 900$ K. This drop in PF/τ is caused by the downward trend of S with the temperature at $T > 600$ K for CrFe$_2$O$_4$ doped at carrier concentrations of 10^{19} cm^{-3} (Figure 4b). $S(T)$ is, nonetheless, nearly flat for higher doping levels in CrFe$_2$O$_4$, which indicates this drop is milder for higher doping levels (**Figures S9** and **S10**). For MoFe$_2$O$_4$, σ / τ, PF/τ are generally a few times higher for n doping than for p doping. Furthermore, for both n and p doping, σ / τ and PF/τ vary moderately with temperature, indicating that a reasonably high power factor can be maintained even when the operating temperature varies.

To relate the values presented in Figure 6 to experimental measurements, we should estimate τ. τ can be estimated from experimental carrier mobility (μ) measurements via $\tau = \mu m^* / q$, in which q and m^* are the carrier's charge and
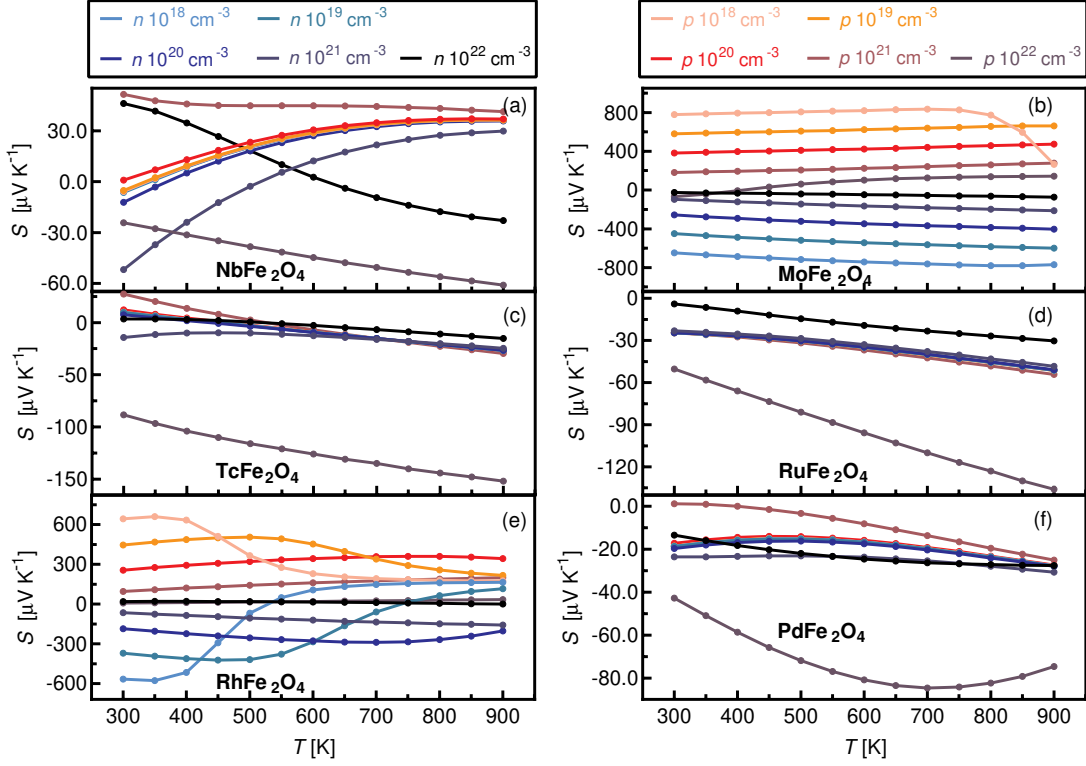
Figure 5. The predicted S values for 4d-based TMFe$_2$O$_4$ compounds as a function of temperature and carrier doping. Panels (a) through (f) correspond to NbFe$_2$O$_4$ through PdFe$_2$O$_4$, respectively, arranged by TM's atomic number.

band effective mass, respectively. For the p-type MoFe$_2$O$_4$, the hole relaxation time (τ_h) has already been measured to be $\sim 10^{-13}$ s at room temperature for polycrystalline bulk samples.[40,60] Based on this τ_h value, κ_e is estimated to be 3.78 mW K^{-1} m^{-1} at $T = 300$ K and 30.14 mW K^{-1} m^{-1} at $T = 900$ K. These values are rather small for typical oxides—for instance, κ_e is ~ 1500 mW K^{-1} m^{-1} for doped SrTiO$_3$ at ambient[61]—indicating the minor role of electrons in heat transport. Furthermore, the room temperature σ is estimated to be 20.37 Ω^{-1} cm^{-1}, which is lower than that of most thermoelectric oxides (**TABLE S1**) and is in par with some other excellent thermoelectric materials such as ReSi$_{1.75}$.[62,63] Higher conductivity can nonetheless be achieved by higher doping level (**Figures S9** and **S10**). The room temperature PF is estimated to be 689.81 µW K^{-2} m^{-1}, which is higher than that of most oxides (**TABLE S1**). Assuming τ_h remains constant with varying temperature, the power factor, at $T = 600$ K, would be 455.67 µW K^{-2} m^{-1}, which only shows a minor drop with respect to the PF value at ambient. Consequently, lightly doped p-type MoFe$_2$O$_4$ is anticipated to be an excellent choice for room and low temperature ($T < 600$ K) applications.

Although Figure 6 indicates that σ / τ and PF/τ are ~ 6 times higher for n-doped MoFe$_2$O$_4$ than the p-doped compound, σ, and PF themselves may not be this high. That is because τ for electrons and holes is quite different and critically depends on the band effective mass. The band effective hole and electron masses, for MoFe$_2$O$_4$, are 0.45m_0 and 2.52m_0, respectively, as calculated in **Figures S11**–**S13**, and **TABLE S2** (m_0 is electron mass at rest). Given that electrons are ~ 5 times heavier than holes, we should be somewhat conservative in predicting the thermoelectric performance of the n-type MoFe$_2$O$_4$. The same forecast is also valid for CrFe$_2$O$_4$ for which the electron effective mass is ~ 5 times heavier than the hole effective mass.

Both CrFe$_2$O$_4$ and MoFe$_2$O$_4$ have been experimentally synthesized, and optically and electronically characterized, indicating their feasibility for thermoelectric applications.[40,64] Here, we further investigate the dynamic stability of these compounds. A material is dynamically stable if it passes the Born-Huang criteria.[65] These criteria state that the Gibbs free energy of any stable crystal is minimum compared to any other state induced by an infinitesimal strain. Fulfilling this requires that the 6×6 elastic stiffness matrix C_{ij} to be positive definite, that is, all the eigenvalues of C_{ij} are positive, while the C_{ij} matrix itself is symmetric. Furthermore, for the cubic systems, such as the spinel structure, the following criteria must also be met: $C_{11} - C_{12} > 0$; $C_{11} + 2C_{12} > 0$; and $C_{44} > 0$.[66] Table I shows the unique non-zero stiffness matrix elements for CrFe$_2$O$_4$ and MoFe$_2$O$_4$, along with the corresponding Debye temperatures (θ_D).
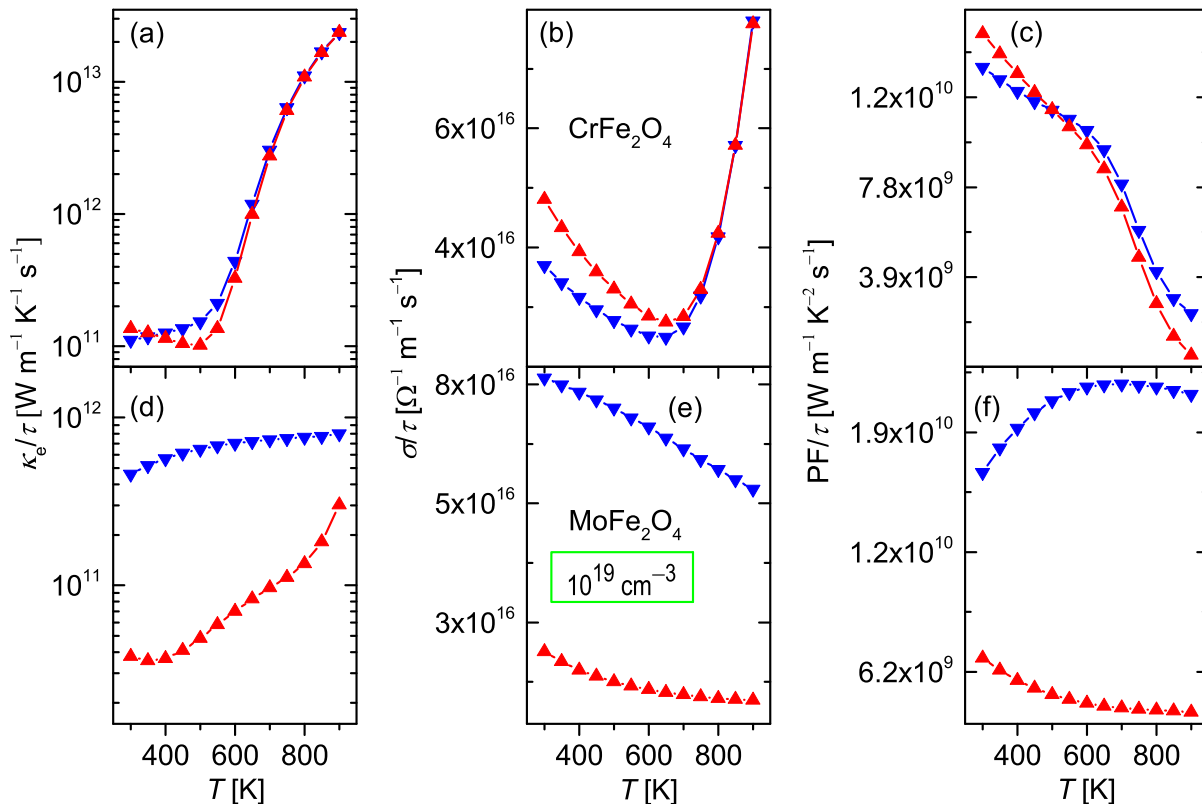
Figure 6. Upper row panels show the electronic contribution to the thermal conductivity per relaxation time (κ_e / τ) (a), the electric conductivity per relaxation time (σ / τ) (b), and the power factor per relaxation time (PF/τ) (c) for $CrFe_2O_4$. The lower row panels (d), (e), and (f) show the same quantities for $MoFe_2O_4$. Red and blue symbols indicate hole and electron doping, respectively. The carrier concentration is 10^{19} carriers/cm^3.

TABLE I. The unique nonzero elements of the stiffness matrix along with the Debye temperature for $CrFe_2O_4$ and $MoFe_2O_4$.

	$CrFe_2O_4$	$MoFe_2O_4$
C_{11} (GPa)	230.09	175.48
C_{12} (GPa)	135.94	127.40
C_{44} (GPa)	69.87	59.20
θ_D (K)	523.36	405.23

Both of these compounds meet the Born stability criteria.

Finally, we would like to draw attention to the experimentally important fact that all investigated compounds here were of spinel structure in which all non-iron TM ions (except for Fe_3O_4) were at the tetrahedral site (A site). Often, the site preference of the non-iron cation in ferrites depends on the synthesis method. In extreme cases where all the non-iron cations are located at the octahedral site (B site), the structure is referred to as an inverse spinel. In reality, any given spinel ferrite may be in an in-between case characterized by an inversion parameter. For instance, $\sim$ 60 nm thick $MoFe_2O_4$ deposited on $MgAl_2O_4$ [100] by pulsed laser deposition has an inverse spinel structure.[67] Mo's site preference in polycrystalline bulk samples could, nonetheless, be tuned by the sintering temperature.[40] The higher the sintering temperature was, the more likely Mo occupied the tetrahedral site. Generally, the site preference of the different cations in spinels can be fine-tuned by adjusting the strain (lattice mismatch)[68], self-doping[69] and

annealing[70] in thin films; and selecting suitable precursors,[71] sintering temperature[40] and nano-structuring[72] in bulk samples. The wealth of the experimental know-how in synthesizing ferrites can undoubtedly come handy in developing thermoelectric $TMFe_2O_4$, especially for nanostructuring as a mean of reducing the lattice thermal conductivity and enhancing thermoelectric response.[33]

IV. CONCLUSIONS

Using density functional band structure calculations and linearized Boltzmann transport equation, we surveyed the thermoelectric properties of twelve ferrite compounds of $TMFe_2O_4$ composition with spinel structure in which TM was either a 3d or 4d transition metal cations. We demonstrated that the absolute value of the Seebeck coefficient, at ambient conditions, can exceed ± 600 µV K^{-1} in $CrFe_2O_4$, $MnFe_2O_4$, $MoFe_2O_4$, and $RhFe_2O_4$ when lightly doped with electrons and holes at concentrations smaller than 10^{20} carriers/cm^3. Additionally, in these compounds, S is the highest at room temperature and tapers off very moderately with rising temperatures up to 600 K. This behavior is starkly different from that of most thermoelectric oxides for which S is minuscule at ambient and only becomes significant at temperatures higher than 800 K. Consequently, for p-type $MoFe_2O_4$ the thermoelectric power factor can reach 689.81 µW K^{-2} m^{-1} at 300 K, and 455.67 µW K^{-2} m^{-1} at 600 K. The unusually high S for $CrFe_2O_4$ and $MoFe_2O_4$ is caused by the Fe^{2+}'s sharp density of states peak in the minority spin channel just below the valence band maximum. The analysis performed here, by contributing to the understanding of thermoelectrics properties of oxides, will facilitate more extensive use of this class of materials for applications close to room temperature.

V. CONFLICTS OF INTEREST

The authors declare that there is no conflict of interest.

VI. ACKNOWLEDGMENTS

VII. SUPPORTING INFORMATION

Validity tests for the applied U and J values, S vs. μ plots at different temperatures and as a function of the shift in the chemical potential, thermoelectric transport for VFe_2O_4 at 10^{19} carriers per cm^3 doping, $CeFe_2O_4$ and $MoFe_2O_4$ at 10^{20} and 10^{21} carriers per cm^3 doping, comparison of the thermoelectric performance with other oxides, the procedure for calculating the effective masses.

* h.assadi.2008@ieee.org

[1] G. J. Snyder and E. S. Toberer, Nat. Mater. **7**, 105 (2008).

[2] J. W. Fergus, J. Eur. Ceram. Soc. **32**, 525 (2012).

[3] Y. Liu, W. Wang, J. Yang, and S. Li, Adv. Sustain. Syst. **2**, 1800046 (2018).

[4] S. LeBlanc, Sustain. Mater. Technol. **1–2**, 26 (2014).

[5] L. V. G. Fachini, P. L. O. Machado, L. Krambeck, R. M. Szmoski, and T. A. Alves, "Heat recovery and power generation using thermoelectric generator," in *Thermoelectrics for Power Generation*, edited by S. Memon (IntechOpen, 2019).

[6] S. Zhang, E. Laboure, D. Labrousse, and S. Lefebvre, in *PCIM Europe 2018; International Exhibition and Conference for Power Electronics, Intelligent Motion, Renewable Energy and Energy Management* (2018) pp. 1–8.

[7] G. Zhang and Y.-W. Zhang, J. Mater. Chem. C **5**, 7684 (2017).

[8] G. J. Snyder, Y. Tang, C. M. Crawford, and E. S. Toberer, "Recent progress in skutterudites," in *Materials Aspect of Thermoelectricity* (CRC Press, 2016) pp. 533–554.

[9] T. Zhu, C. Fu, H. Xie, Y. Liu, and X. Zhao, Adv. Energy Mater. **5**, 1500588 (2015).

[10] W. G. Zeier, J. Schmitt, G. Hautier, U. Aydemir, Z. M. Gibbs, C. Felser, and G. J. Snyder, Nat. Rev. Mater. **1**, 16032 (2016).

[11] L. Huang, Q. Zhang, B. Yuan, X. Lai, X. Yan, and Z. Ren, Mater. Res. Bull. **76**, 107 (2016).

[12] A. Nozariasbmarz, A. Agarwal, Z. A. Coutant, M. J. Hall, J. Liu, R. Liu, A. Malhotra, P. Norouzzadeh, M. C. ztrk, V. P. Ramesh, Y. Sargolzaeiaval, F. Suarez, and D. Vashaee, Jpn. J. Appl. Phys. **56**, 05DA04 (2017).

[13] Y. Lan, D. Wang, and Z. Ren, "Silicon–germanium alloys," in *Advanced Thermoelectrics*, edited by Z. Ren, Y. Lan, and Z. Qinyong (CRC Press, 2017) pp. 353–370.

[14] A. Bohra, R. Bhatt, S. Bhattacharya, R. Basu, S. Ahmad, A. Singh, D. Aswal, and S. Gupta, in *AIP Conf. Proc.*, Vol. 1731 (AIP Publishing, 2016) p. 110010.

[15] W. Shi, M. Gao, J. Wei, J. Gao, C. Fan, E. Ashalley, H. Li, and Z. Wang, Adv. Sci. **5**, 1700602 (2018).

[16] L. Bjerg, G. K. H. Madsen, and B. B. Iversen, Chem. Mater. **24**, 2111 (2012).

[17] K. Niedziolka, R. Pothin, F. Rouessac, R. M. Ayral, and P. Jund, J. Phys. Condens. Matter **26**, 365401 (2014).

[18] J.-i. Tani and H. Kido, Physica B **364**, 218 (2005).

[19] R. Amatya and R. J. Ram, J. Electron. Mater. **41**, 1011 (2012).

[20] M. Lorenz, M. S. Ramachandra Rao, T. Venkatesan, E. Fortunato, P. Barquinha, R. Branquinho, D. Salgueiro, R. Martins, E. Carlos, A. Liu, F. K. Shan, M. Grundmann, H. Boschker, J. Mukherjee, M. Priyadarshini, N. DasGupta, D. J. Rogers, F. H. Teherani, E. V. Sandana, P. Bove, K. Rietwyk, A. Zaban, A. Veziridis, A. Weidenkaff, M. Muralidhar, M. Murakami, S. Abel, J. Fompeyrine, J. Zuniga-Perez, R. Ramesh, N. A. Spaldin, S. Ostanin, V. Borisov, I. Mertig, V. Lazenka, G. Srinivasan, W. Prellier, M. Uchida, M. Kawasaki, R. Pentcheva, P. Gegenwart, F. Miletto Granozio, J. Fontcuberta, and N. Pryds, J. Phys. D: Appl. Phys. **49**, 433001 (2016).

[21] M. Haras and T. Skotnicki, Nano Energy **54**, 461 (2018).

[22] B. Orr, A. Akbarzadeh, M. Mochizuki, and R. Singh, Appl. Thermal Eng. **101**, 490 (2016).

[23] Y. Feng, X. Jiang, E. Ghafari, B. Kucukgok, C. Zhang, I. Ferguson, and N. Lu, Adv. Compos. Hybrid Mater. **1**, 114 (2018).

[24] D. Champier, Energy Convers. Manag. **140**, 167 (2017).

[25] S. Curtarolo, G. L. W. Hart, M. B. Nardelli, N. Mingo, S. Sanvito, and O. Levy, Nat. Mater. **12**, 191 (2013).

[26] M. H. N. Assadi and H. Katayama-Yoshida, Comput. Mater. Sci. **109**, 308 (2015).

[27] P. Gorai, D. Gao, B. Ortiz, S. Miller, S. A. Barnett, T. Mason, Q. Lv, V. Stevanovi, and E. S. Toberer, Comput. Mater. Sci. **112**, 368 (2016).

[28] M. Assadi, S. Li, R. Zheng, S. Ringer, and A. Yu, Chem. Phys. Lett. **687**, 233 (2017).

[29] P. Gorai, V. Stevanovi, and E. S. Toberer, Nat. Rev. Mater. **2**, 17053 (2017).

[30] M. Mukherjee and A. K. Singh, ACS Appl. Mater. Interfaces **12**, 8280 (2020).

[31] A. Bouhemadou, D. Allali, K. Boudiaf, B. Al Qarni, S. Bin-Omran, R. Khenata, and Y. Al-Douri, J. Alloys Compd. **774**, 299 (2019).

[32] R. S. S. Maki, S. Mitani, and T. Mori, Mater. Renew. Sustain. Energy **6**, 2 (2016).

[33] F. Azough, A. Gholinia, D. T. Alvarez-Ruiz, E. Duran, D. M. Kepaptsoglou, A. S. Eggeman, Q. M. Ramasse, and R. Freer, ACS Appl. Mater. Interfaces **11**, 32833 (2019).

[34] G. Kresse and D. Joubert, Phys. Rev. B **59**, 1758 (1999).

[35] G. Kresse and J. Furthmller, Phys. Rev. B **54**, 11169 (1996).

[36] G. Kresse and J. Furthmller, Comput. Mater. Sci. **6**, 15 (1996).

[37] S. Dudarev, G. Botton, S. Savrasov, C. Humphreys, and A. Sutton, Phys. Rev. B **57**, 1505 (1998).

[38] A. I. Liechtenstein, V. I. Anisimov, and J. Zaanen, Phys. Rev. B **52**, R5467 (1995).

[39] M. Fonin, Y. S. Dedkov, R. Pentcheva, U. Rdiger, and G. Gntherodt, J. Phys. Condens. Matter **19**, 315217 (2007).

[40] A. Ramdani, C. Gleitzer, G. Gavoille, A. K. Cheetham, and J. B. Goodenough, J. Solid State Chem. **60**, 269 (1985).

[41] P. Gopal and N. A. Spaldin, Phys. Rev. B **74**, 094418 (2006).

[42] M. H. N. Assadi and H. Katayama-Yoshida, J. Phys. Soc. Jpn. **88**, 044706 (2019).

[43] X. Wu, D. Vanderbilt, and D. Hamann, Phys. Rev. B **72**, 035105 (2005).

[44] S. Singh, I. Valencia-Jaime, O. Pavlic, and A. H. Romero, Phys. Rev. B **97**, 054108 (2018).

[45] G. K. H. Madsen, J. Carrete, and M. J. Verstraete, Comput. Phys. Commun. **231**, 140 (2018).

[46] T. Scheidemantel, C. Ambrosch-Draxl, T. Thonhauser, J. V. Badding, and J. O. Sofo, Phys. Rev. B **68**, 125210 (2003).

[47] W. Chen, J.-H. Phls, G. Hautier, D. Broberg, S. Bajaj, U. Aydemir, Z. M. Gibbs, H. Zhu, M. Asta, G. J. Snyder, B. Meredig, M. A. White, K. Persson, and A. Jain, J. Mater. Chem. C **4**, 4414 (2016).

[48] D. Szmyd, M. Hanna, and A. Majerfeld, J. Appl. Phys. **68**, 2376 (1990).

[49] M. L. Lovejoy, M. R. Melloch, and M. S. Lundstrom, Appl. Phys. Lett. **67**, 1101 (1995).

[50] D. J. Singh, Phys. Rev. B **81**, 195217 (2010).

[51] B. Xu and M. J. Verstraete, Phys. Rev. Lett. **112**, 196603 (2014).

[52] D. J. Singh, Phys. Rev. B **61**, 13397 (2000).

[53] E. Levin, Phys. Rev. B **93**, 245202 (2016).

[54] K. Mori, H. Sakakibara, H. Usui, and K. Kuroki, Phys. Rev. B **88**, 075141 (2013).

[55] S. Yabuuchi, M. Okamoto, A. Nishide, Y. Kurosaki, and J. Hayakawa, Appl. Phys. Express **6**, 025504 (2013).

[56] J.-R. Huang and C. Cheng, J. Appl. Phys. **113**, 033912 (2013).

[57] S. E. Shirsath, X. Liu, M. H. N. Assadi, A. Younis, Y. Yasukawa, S. K. Karan, J. Zhang, J. Kim, D. Wang, A. Morisako, Y. Yamauchi, and S. Li, Nanoscale Horiz. **4**, 434 (2019).

[58] H.-W. Jeon, H.-P. Ha, D.-B. Hyun, and J.-D. Shim, J. Phys. Chem. Solids **52**, 579 (1991).

[59] M. Takashiri, T. Shirakawa, K. Miyazaki, and H. Tsukamoto, Sens. Actuator A Phys. **138**, 329 (2007).

[60] M. P. Gupta, A. P. B. Sinha, S. M. Kanetkar, S. K. Date, and A. S. Nigavekar, J. Phys. C Solid State Phys. **12**, 2401 (1979).

[61] N. Wang, H. Chen, H. He, W. Norimatsu, M. Kusunoki, and K. Koumoto, Sci. Rep. **3**, 3449 (2013).

[62] U. Gottlieb, B. LambertAndron, F. Nava, M. Affronte, O. Laborde, A. Rouault, and R. Madar, J. Appl. Phys. **78**, 3902 (1995).

[63] H. Inui, Mater. Res. Soc. Symp. Proc. **886**, 0886 (2005).

[64] S. A. Chambers, T. C. Droubay, T. C. Kaspar, I. H. Nayyar, M. E. McBriarty, S. M. Heald, D. J. Keavney, M. E. Bowden, and P. V. Sushko, Adv. Funct. Mater. **27**, 1605040 (2017).

[65] M. Born and K. Huang, Am. J. Phys. **23**, 474 (1955).

[66] F. Mouhat and F.-X. Coudert, Phys. Rev. B **90**, 224104 (2014).

[67] T. Katayama, Y. Kurauchi, S. Mo, K. Gu, A. Chikamatsu, L. Galiullina, and T. Hasegawa, Cryst. Growth Des. **19**, 902 (2018).

[68] D. Fritsch and C. Ederer, Appl. Phys. Lett. **99**, 081916 (2011).

[69] N. Bahlawane, P. H. T. Ngamou, V. Vannier, T. Kottke, J. Heberle, and K. Kohse-Hinghaus, Phys. Chem. Chem. Phys. **11**, 9224 (2009).

[70] P. F. Ndione, Y. Shi, V. Stevanovic, S. Lany, A. Zakutayev, P. A. Parilla, J. D. Perkins, J. J. Berry, D. S. Ginley, and M. F. Toney, Adv. Funct. Mater. **24**, 610 (2014).

[71] K. Petrov, L. Markov, R. Ioncheva, and P. Rachev, J. Mater. Sci. **23**, 181 (1988).

[72] Q. Song and Z. J. Zhang, J. Am. Chem. Soc. **134**, 10182 (2012).